Diffraction signatures of fracture intersections

Mark Grasmueck[1], Tijmen Jan Moser[2], Michael A. Pelissier[3], Jan Pajchel[4], and Kenri Pomar[5]

Abstract

Fractured rock causes diffractions, which are often discarded as noise in ground-penetrating radar (GPR) and seismic data. Most fractures are too thin, too steep, and their displacement is too small to be imaged by reflections, and diffractions are the only detectable signal. To decipher the information about fracture geometry and distribution contained in diffractions, we compare 3D synthetic ray-Born modeling with high-density 3D GPR data and outcrop observations from the Cassis Quarry in Southern France. Our results reveal how the intersection between two fractures is the basic geologic element producing a recordable diffraction. In this new model, two intersecting fractures are represented by one finite-length line diffractor. The intersection of three fractures is a 3D cross composed of three line diffractors. Fractures extending over several meters in the outcrop display linear clusters of diffraction circles in unmigrated GPR time slices. Such large-scale fracture intersections are composed of many aligned short subwavelength line diffractors due to fracture roughness and variations of fracture opening. The shape irregularities and amplitude variations of composite diffraction signatures are a consequence of the geometry and spacing of the intersecting fractures generating them. With three simple base-type intersecting fracture models (horizontal dip, gentle dip, and steep dip), the fracture network geometry can be directly deciphered from the composite diffraction signatures visible on unmigrated time slices. The nonrandom distribution of diffractions is caused by fracture trends and patterns providing information about fracture dip, spacing, and continuity of fractured domains. With the similarity law, the diffraction phenomena observed in GPR data are very similar in character to those seen on the seismic scale with the wavelength as the scaling link. GPR data serve as a proxy to decipher seismic diffractions.

Introduction

The seismic reflection method is optimized toward imaging of continuous reflectors to delineate stratigraphic boundaries. However, the productivity of many conventional and unconventional reservoirs is governed by small-scale discontinuities such as fractures or voids. As a consequence, seismic reflection interpretation is of limited use for characterization of discontinuous reservoirs and drilling success rates are lower than for continuous stratigraphic reservoirs. Reservoir production and stimulation would also benefit from laterally extensive information about connected fracture networks. Typically, subvertical fracture mapping relies on detecting subtle edges of otherwise continuous reflections. Semblance or coherency attributes help make such edges visible (Marfurt et al., 1998). In theory, vertical displacements larger than a quarter wavelength of the highest frequency are resolvable for the seismic reflection method. Fractures with smaller or zero vertical displacement are beyond the resolution of classical reflection seismic fracture mapping. Borehole imaging and structural modeling may help estimate the distribution of smaller fractures but are limited by spatial uncertainty. Seismic anisotropy (Questiaux et al., 2010) and emissions of acoustic energy during reservoir stimulation and depletion (Geiser et al., 2012) can help gain information on fractures systems not resolved by reflection seismic imaging.

Diffraction signals are a direct expression of subsurface heterogeneity. On seismic records, subwavelength scale void and fracture discontinuities cause diffractions and produce scattered energy. Such scattering is commonly regarded as noise and suppressed during seismic acquisition and processing: diffractions interfere with continuous reflections and have weak amplitudes (Khaidukov et al., 2004). An advantage of

[1]University of Miami, Center for Carbonate Research (CSL), Miami, Florida, USA. E-mail: mgrasmueck@rsmas.miami.edu.
[2]Moser Geophysical Services, The Hague, The Netherlands. E-mail: mosertj@gmail.com.
[3]Presently Roc Oil (Bohai) Company, Beijing, China; formerly Marathon Oil company, Houston USA. E-mail: mike.pelissier@chn.rocoil.com.au.
[4]Statoil Research Center, Bergen, Norway. E-mail: jpajc@statoil.com.
[5]Currently Saudi Aramco, Dhahran, Saudi Arabia; formerly University of Miami, Center for Carbonate Research (CSL), Miami, Florida, USA. E-mail: kenri_p@yahoo.com.

Manuscript received by the Editor 22 April 2014; revised manuscript received 17 August 2014; published online 29 December 2014; corrected version published online 3 February 2015.This paper appears in *Interpretation*, Vol. 3, No. 1 (February 2015); p. SF55–SF68, 14 FIGS., 1 TABLE.
http://dx.doi.org/10.1190/INT-2014-0086.1.

diffraction analysis and imaging is that it is done before stack and migration, in contrast to the analysis of coherency and semblance attributes. Diffractions already have been successfully used to define oil-bearing karst caverns which previously had not been resolved (Yang et al., 2011). A geologically plausible model for the origin of karst diffractions with subwavelength spherical or random bodies of low-velocity material (2500–3200 m/s) embedded in high-velocity cemented carbonate host rock (6000 m/s) is proposed by Li et al. (2012).

Diffractions are also a promising source for subwavelength 3D fracture information. For example, work by Landa et al. (1987) and Pant et al. (1992) demonstrates pushing the detection limit for small-scale faults in exploration seismic data. Similarly, Grasmueck et al. (2013) show how diffractions recorded in dense 3D ground-penetrating radar (GPR) data can be used to image complex karst and fracture networks.

The objective of this paper is to find a geologic model for the origin of diffractions in fractured rock formations in which no voids are present. With the knowledge of the typical diffraction signatures caused by elementary fracture intersection models, the subwavelength 3D fracture network information contained in scattered energy can be deciphered.

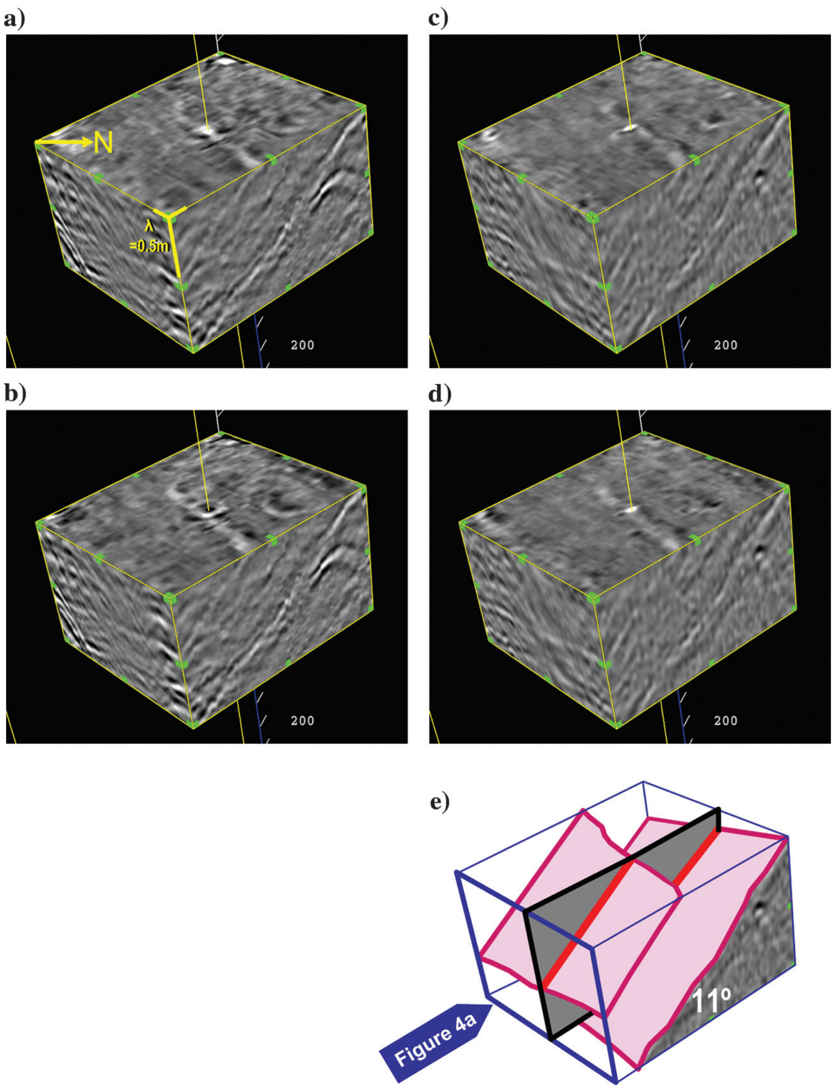

Figure 1. Subvolume of larger 3D GPR survey acquired in the Cassis Quarry (France). The bright spot in the center of the top face is caused by the intersection of a vertical with a subhorizontal fracture. Panels (a and b) are unmigrated data. In panel (b), the top face is 5 cm deeper than in panel (a) showing circular diffraction pattern. Panels (c and d) are the corresponding 3D migrated cubes where the diffraction hyperboloid has been focused into a small high-amplitude anomaly. (e) Fracture interpretation. The red lines mark fracture intersections. The depth conversion velocity v is 0.0975 m/ns. The blue arrow indicates the viewing direction in Figure 4a.

Hypothesis and approach

The Cassis Quarry fractured carbonate reservoir analog

Fractured Cretaceous limestones are outcropping in an abandoned quarry near the village of Cassis in southern France (Masse et al., 2003). The 1500 m of exposed quarry walls and more than 50,000 m^2 accessible quarry floor area enable direct comparison and verification of full-resolution 3D GPR responses with outcropping fracture networks. *Fracture* is a general term referring to the breaking of rock and creating free surfaces. The quarry outcrops are dominated by subhorizontal and steep dipping joints, which are fractures with no displacement across the fracture surfaces and are caused by extensional deformation. Faults or fractures with significant lateral displacement are rare in the quarry.

Figure 1 displays a small subvolume of the larger Cassis 3D GPR survey acquired with 5×10 cm trace spacing and 200 MHz antennae (Grasmueck et al., 2013). The low-amplitude 11° dipping subhorizontal reflections are caused by around 1 mm open joints following stratigraphic boundaries. When following the reflection bands of these subhorizontal fractures in time slices, it appears that they are lined by small bright spots. The center of the time slice in Figure 1a is located on such a bright spot. On unmigrated data, the bright spot corresponds to the apex of a diffraction cone. For a slightly deeper time slice, the spot has the shape of a circle (Figure 1b). In the 3D migrated data in Figure 1c and 1d, the diffraction is focused in a small and elongated high-amplitude anomaly. The long axis of the migrated anomaly is aligned with the intersection line between the two joints (Figure 1e). Within the entire 3D GPR survey volume, hundreds of such small bright spots can be observed. Laterally extensive fractures are defined by several such bright spots aligned in the same fracture plane (Grasmueck et al., 2013).

Our hypothesis is that recorded diffractions can be caused by fracture intersections. We use high-resolution 3D GPR data as a bridge between synthetic modeling and seismic reservoir imaging. Natural fracture networks of outcropping reservoir analogs can be efficiently imaged with 3D GPR and interpreted with help of the nearby outcrop. Due to the kinematic similarity of electromagnetic and seismic wave propagation, the GPR data can be used as a proxy for seismic data to help develop new diffraction based fracture imaging work flows. Through scaling relationships, the diffraction phenomena at GPR scale can be related to diffraction phenomena at seismic scale (for seismic scattering by a crack, see, e.g., Sánchez-Sesma and Iturrarán-Viveros, 2001). We note that we study only zero-offset stacked data in this paper. The GPR data are acquired by near zero offset transmitter-receiver pairs. The equivalent seismic data modality is the brute stack incorporating only signals in a small offset range.

Full-resolution 3D ground-penetrating radar imaging

GPR uses electromagnetic waves but has very similar kinematic and dynamic properties in terms of reflection, refraction, and diffractions to those of seismic waves. By acquiring very dense 3D GPR data with a grid spacing of less than quarter-wavelength in all directions and properly sampling diffractions, we have been able to produce images of fractures and karst networks with unprecedented resolution and clarity (Grasmueck et al., 2005, 2013). The key to producing these images was 3D migration processing to collapse the diffractions. The new work presented in this paper analyzes the unmigrated signatures of diffractions. The objective is to better understand the origin of diffractions and investigate their information content in terms of fracture geometry and distribution. Deciphering and verifying the signatures of raw diffractions is supported by ray-Born synthetic modeling (see the next section) reproducing the diffraction patterns observed in the 3D GPR field data. The combined findings from modeling and full-resolution 3D GPR data can be used to inspire new seismic surveying, processing, and interpretation practices for improved characterization of fractured reservoirs.

Ray-Born synthetic modeling

Ray-Born modeling is a hybrid technique for the forward modeling of first-order scattered waves that consists of ray tracing in a smooth background model and the Born integral for scattering on a small perturbation of the background model (see Moser, 2010, 2012). It combines the advantages of ray tracing and the Born integral: computational speed in the background model and no limiting assumptions on the integrability of the scatterer. This means that scatter geometries of considerable complexity can be handled, in many cases models that pose serious difficulties for other forward-modeling techniques. The assumptions of the ray-Born approximation are a smooth (ray-tracing-friendly) background model and a weak scatterer. In this paper, we take for the background a constant velocity model which is representative for the Cassis Quarry; in such a model, the rays are straight lines and traveltimes and amplitudes along them can be evaluated by simple analytical formulas. The scatterer models (fracture intersections) consist of point scatterers of unit scattering strength arranged in lines with uniform and sufficient density so that summation over them is equivalent to the scattering integral. The fact that the ray-Born approximation underlies most migration algorithms and therefore shares their assumptions is a justification in itself to consider it for forward modeling. In this paper, we consider only first-order Born scattering. Higher order (multiple) scattering can be included easily, but at the expense of a higher computation burden, whereas the amplitude of higher order scattering is typically an order of magnitude smaller than the primary scattering. Thanks to its hybrid nature, ray-Born modeling allows use of a relatively sparse grid for the background model and a hyperfine grid for the scatter target. There are therefore in principle no numerical limits to the resolution of the modeled wave and no numerical artifacts such as dispersion or grid diffractions. By contrast, finite differences require either a very dense global grid and very small time step or an elaborate adaptive grid scheme, which is often prohibitive in three dimensions (Thore et al., 2009; Thore and Tarrass, 2010). Because the Born scattering integral does not distinguish between specular reflections and nonspecular diffractions, reflected and diffracted waveforms and amplitudes are computed with uniform accuracy, including the edge and tip diffractions.

Line diffractor: Intersection of two fracture planes

Diffractions originate from subwavelength discontinuities such as points, edges, and corners. The superposition of point diffractions gives rise to edge and tip waves but also the full diffraction response caused by discontinuities of any shape. In this paper, we use straight-line diffractors as the basic building blocks to represent fracture intersections; in doing this, we were inspired by the strip diffraction modeling presented by Dong et al. (1999). The elementary line diffractor may be oriented in three dimensions, with an arbitrary dip and azimuth. Line diffractors may be organized into sets to represent, for example, the intersection of a set of subhorizontal fractures with a single subvertical fracture (Figure 1e). Another important example is the intersection of three fractures, which can be represented by a set of three line diffractors arranged in a 3D cross discussed in the next section.

The elementary line diffractor represents the intersection of two fracture planes. The geometry for the simplest case is shown in Figure 2a. This is for the intersection of a vertical fracture plane with a horizontal fracture plane, forming a horizontal line of intersection. The geometry of the diffracted rays is indicated by arrows. At any point on the line, these rays are limited to the plane perpendicular to the line (colored in blue). The associated diffraction response forms a hyperbola in this plane. The contributions along the line form a string of hyperbolae, reminiscent of an anticlinal structure with a hyperbolic cross section. The analogy to an anticline is useful from an interpretation viewpoint. As we will show later, a dipping line diffractor produces a response similar to the reflection response of a plunging anticline. At either end of the line, the rays travel in all directions (colored in green). The traveltime pattern is that of a point diffractor.

A time slice of the diffraction response of this elementary line diffractor is shown in Figure 2b. Here, the linear features are the flanks of the diffraction hyperbolae forming the above-mentioned anticlinal structure. The diffractions from the ends of the line have the familiar circular response of a point diffractor. An important distinction, however, is the polarity reversal characteristic for the tip wave. The exterior halves of the circles have the same polarity as the hyperbolic flanks, whereas the polarity of the interior halves is reversed.

Representative time slices from the GPR data are shown in Figure 2c and 2d. Here, we can observe strings of circular diffraction patterns, with the diameter increasing with depth. A simple comparison with the basic line diffractor response makes it clear that extended lines of intersection do not exist in the diffraction response of naturally fractured rocks. The linear arrangement of closely spaced diffraction circles with similar radii in Figure 2c is interpreted as the response of a broken line consisting of several very short horizontal line diffractors. On a slightly deeper time slice (Figure 2d), the circles are transformed into mirrored half-circles with a low-amplitude corridor in between. Destructive interference between neighboring point diffractions causes the low-amplitude corridor and creates mirrored half-circle signatures. A denser spacing of the point diffractions along a line would produce the ideal linear diffraction shown in Figure 2b.

Let us now examine the effect of the line diffractor length on the diffraction response. In Figure 3, we present the model response of horizontal line diffractors ranging in length from $\lambda/8$ to 4λ, where λ is the wavelength. The background model has a constant velocity. The cross section shown in Figure 3a is in the same plane as the line diffractors. As the line length decreases in Figure 3a, the diffractions from the ends of the line merge to form a response resembling that of a vertical section in the plane of a point diffractor. The amplitude strength of the short line diffraction responses increases with line diffractor length. For line lengths larger than one wavelength, we observe in Figure 3a the splitting of the diffraction tails into two parallel events with opposite polarity. These tip waves form two circles in the time slice of Figure 3b at the ends of the line diffractor. The two circles are connected by short linear flanks. For a line length of $\lambda/4$, the line diffractor response reduces to a single point diffractor circle. The double-ring signature from the 3D GPR data shown in Figure 3c resembles the 4λ synthetic data, but the linear flanks are not evident. Also in Figure 2c, no linear flanks can be observed, although strings of diffraction circles or mirrored half-circles are common. This leads to the conclusion that the line diffractors formed by natural fracture intersections must be shorter than the GPR wavelength of 0.5 m with GPR signatures resembling point diffractions. The diffraction signature shown in Figure 2c is composed of 10-point diffractions distributed over a 5.4-m horizontal distance. Therefore, the average spacing of the imaged fracture intersections is 0.6 m or 1.2λ. The time slice showing the diffraction circles is one to two periods below the scatterers. Similarly, the modeled time slice of the 30λ long line diffractor in Figure 2b is extracted two periods below the apex. The mirrored half-circle signatures in Figure 2d are seen 6 to 10 periods below the apexes.

In summary, the GPR field data show that natural fracture intersections are not long, continuous straight lines but consist of broken lines composed of

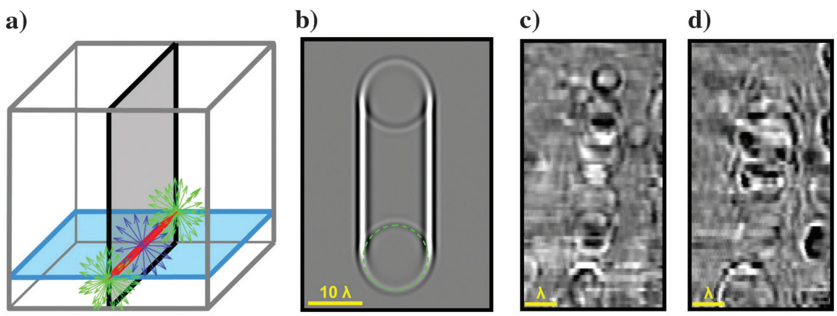

Figure 2. (a) Conceptual model of the intersection of a vertical and horizontal fracture creating a line diffractor (red). The geometry of the diffracted rays is indicated by blue and green arrows. The rays emanating from the ends of the line diffractor are the tipwave. (b) 3D ray-Born synthetic data of 30λ long line diffractor at a depth of 20λ, with $\lambda = 100$ m. The time slice is extracted two signal periods $= 100$ ms two-way time $(= 1\lambda)$ below the line diffractor. The model background velocity of 2000 m/s is used for depth conversion. The green circle visualizes the polarity reversal typical for tip diffractions. (c) Cassis 3D GPR data: The closely spaced circular diffractions have no linear flanks in between. There are a total of 10 diffractors with an average spacing of 0.6 6.0 m $= 1.2\lambda$. The time slice is extracted one to two periods below the scatterers (depth conversion velocity $v = 0.0975$ m/ns and $\lambda = 0.5$ m). (d) Deeper time slice of the same diffraction cluster shows mirrored half-circles with a low-amplitude corridor due to destructive interference in between. The slice is 6 to 10 periods below the scatterers.

linear diffractors with lengths of a wavelength or less. Fractures extending over several meters in outcrop display linear clusters of diffraction circles in unmigrated GPR time slices. Such large-scale fracture intersections are composed of many aligned short subwavelength line diffractors due to fracture roughness and variations of fracture opening. The clearest diffraction signatures with closed circles are observed about one to four periods below the actual diffractor two-way time.

3D cross diffractor: Intersection of three fracture planes

In the Cassis outcrop wall (Figure 4a), the subhorizontal fractures are continuous over tens of meters and relatively smooth, causing the weak subhorizontal GPR reflection bands seen in Figure 1. In contrast, the vertical fractures consist of multiple segments belonging to the same fracture trend. The fracture opening is typically less than 1 mm, similar to the horizontal fractures. The size of continuous fracture segments is typically less than 0.5 m; thus, they are smaller than the wavelength of the GPR signal. The fracture lengths are an expression of the geomechanical properties of the Cassis limestone and deformation intensity. There is no clear relationship between fracture length and bed thickness in the outcrop. At the intersection of vertical and horizontal fractures, sharp corner geometries are formed leading to a blocky appearance of the quarry wall. The dimensions of these blocks are between 0.1 and 0.5 m, illustrated in Figure 4b. Within the 3D rock volume, the corners form dihedrals for two intersecting fractures, Figure 4c, or trihedrals (also known as cat's eyes or corner reflectors) when three fractures intersect, Figure 4d. Dihedrals and trihedrals are known to be efficient wavefield scatterers. The same geometric configuration is used in retroreflectors for the safety of vehicles and backscattering targets in satellite remote sensing applications (López-Martinez et al., 2005). In seismic reflection imaging, dihedral structures are studied by doubly scattered waves, also called duplex or prismatic waves (Malcolm et al., 2011). In the case of fractured media, the intersection of near-perpendicular fractures creates natural scatterers causing diffractions in GPR and seismic data.

We can represent the three intersecting fracture segments of Figure 4d by three intersecting line diffractors taking into account the limited length of the lines of intersection. A similar construct is known as the 3D Greek cross fractal with a Hausdorff dimension of $\log(6)/\log(2) = 2.585$ (Besicovitch and Ursell, 1937). In Figure 5, we illustrate the diffraction response as a function of the size of the cross. Amplitudes can be compared with the line diffractor responses in Figure 3 because the model and display parameters are

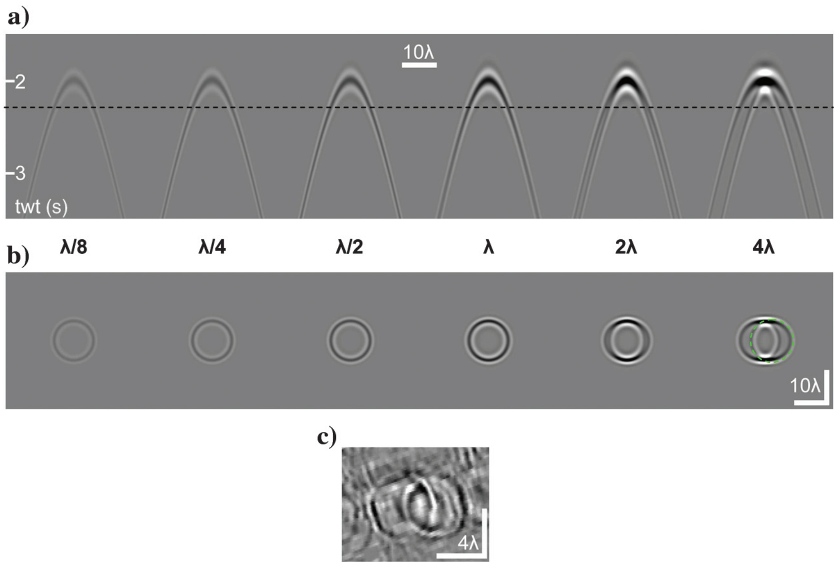

Figure 3. 3D ray-Born synthetic data of horizontal line diffractors with different lengths. The diffractors are buried at 1000 m depth (= 10λ). Model background velocity is 1000 m/s. (a) Vertical section cut through the line diffractors. The dotted line indicates the position of the time slice. (b) Time slice extracted 1.5 periods or 0.75λ below the diffractor depth. The green circle visualizes the polarity reversal typical for tip diffractions. (c) Double-ring signature found in 3D GPR Cassis field data at a depth of 6λ, 0.75λ below the diffraction apices.

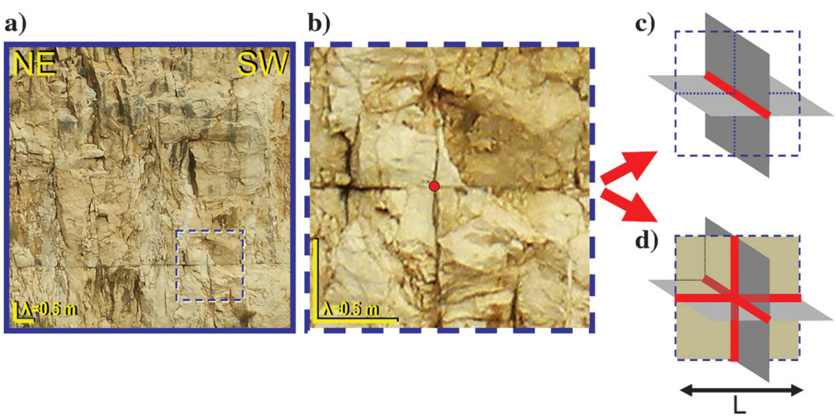

Figure 4. (a) Quarry wall below the site where the 3D GPR data of Figure 1 were acquired. Blocky appearance due to small fracture segments. (b) Zoomed in view of vertical and horizontal fracture intersection. (c) The intersection of two fractures is a linear diffractor (modeled in Figure 3). (d) The intersection of three fractures is a 3D cross (modeled in Figure 5). "L" denotes the line diffractor length modeled in Figures 3 and 5.

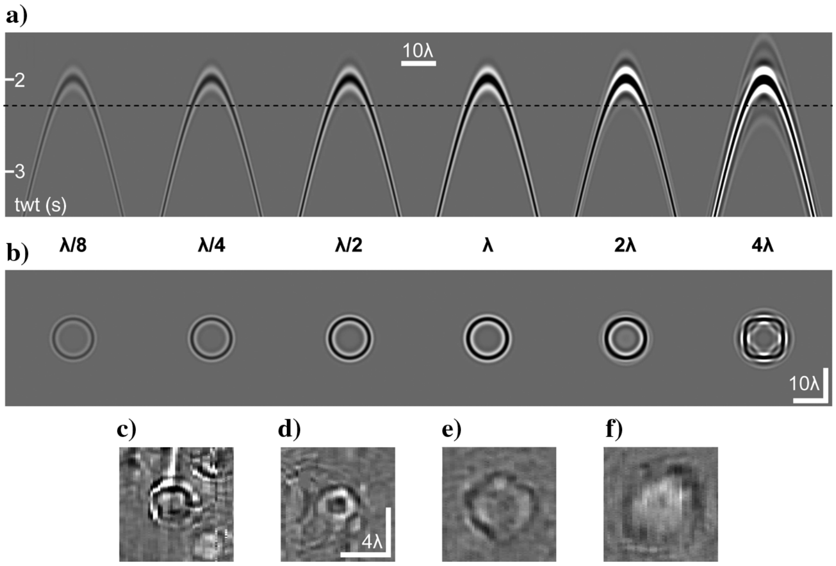

Figure 5. 3D ray-Born synthetic data of 3D crosses with different sizes. The centers of the crosses are buried at 1000 m depth ($= 10\lambda$). Model and display parameters are identical to those in Figure 3, allowing for direct comparisons. (a) Vertical section cut through the centers of the crosses. The dotted line indicates the position of the time slice. (b) Time slice extracted 1.5 periods or 0.75λ below the centers of the crosses. (c) 3D GPR Cassis field data time slice example of square signature a depth of 3λ, 0.5λ below the apex. (d) GPR square signature at depth of 5λ, 0.3λ below the apex, (e) GPR square signature at depth of 12λ, 0.4λ below the apex. (f) GPR square signature at depth of 20λ, 0.4λ below the apex. The horizontal scales on the time slices for (c-f) are the same.

identical. The response in the vertical plane is shown in Figure 5a. A time slice is shown in Figure 5b. As with the individual line diffractors representing the intersection of two fracture planes, we note that for a line length of $\lambda/4$, the response is essentially identical to that of a point diffractor. The relative amplitude of the 3D cross diffractors is stronger than for line diffractors. In the section view for the crosses larger than 1λ, we can observe sets of interfering hyperbolae from the different line diffractors, with a stronger central hyperbola. Weaker hyperbolic events are the tip waves. For the 4λ case, the apex of the topmost hyperbola appears 0.4 s above the center of the cross at the end of the vertical line diffractor element. In the time slices, for the 4λ case, the interference of the various diffraction circles forms a quadratic geometry. Such quadratic time-slice signatures can be observed over the full depth range of the Cassis 3D GPR data (Figure 5c–5f).

Composite diffraction signatures of intersecting fracture sets

The richness and diversity of the Cassis 3D GPR diffraction response are captured in the time slice of Figure 6. Here, we observe that the diffractors are organized in clusters. The perfect diffraction circle seen at $x = 12.5$ m, $y = 42.5$ m is an exception. Diffraction circles rarely have symmetrical amplitudes. In places, we can observe a pattern reminiscent of plunging anticlines on seismic data. Some of the circular features are of a higher amplitude, whereas others appear to be of a much lower amplitude, but with similar radii. Based on the line diffractor building blocks described above, we can now build simple geometric models of intersecting fracture sets to match the character of the composite diffraction patterns observed in the GPR data. For GPR time-to-depth conversions, λ scales, and dip estimates, we use a constant velocity of 0.0975 m/ns and therefore a 0.5-m, 200-MHz GPR wavelength.

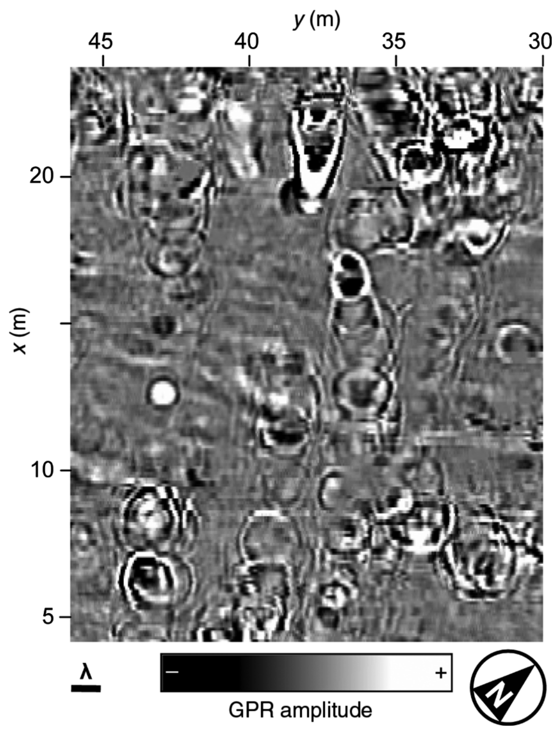

Figure 6. Typical unmigrated Cassis 3D GPR time slice extracted at 1.95 m depth with abundant composite diffraction signatures (assuming depth conversion velocity $v = 0.0975$ m/ns).

Gentle-dip fracture intersections

The introduction of dip into the line diffractor model has an important effect on the diffraction response. The dip direction can be directly interpreted from the diffraction response, much in the way that the plunge of an anticline can be inferred from seismic data. The geometry for a gentle-dip fracture intersection is shown in Figure 7a. A time slice from the model response is shown in Figure 7b, with an arrow indicating the dip direction; this can be readily inferred from the hyperbolic shape on the time slice, as well as the location of the tip wave. The corresponding diffraction pattern observed on the GPR data is shown in Figure 7c.

A composite response caused by a broken line of five adjacent short diffractors is shown in Figure 7d. The average spacing of the diffractors along the fracture intersection is 0.56 m, close to the GPR wavelength. The dip of the fracture intersection as measured between the apexes of the diffraction hyperbolae forming the signatures seen in Figure 7c is 12° and 10° for Figure 7d. A view of the associated outcrop 100 m to the northeast of the 3D GPR survey is shown in Figure 7e. Here, we can observe various short near-vertical fractures intersecting laterally extensive gently dipping fractures with the same dip as measured from the unmigrated diffraction signatures.

Steep-dip fracture intersections

Now, consider a model of steeply dipping fractures extending for some vertical distance, intersected by subhorizontal fractures, as shown in the outcrop in Figure 8a. Although Figures 2d and 7d illustrate the origin of paired symmetrical half-diffractions, the occurrence of single half-circle diffractions (moon shape) shown in Figure 8b is also common. This diffraction signature is caused by vertically stacked diffractions of steeply dipping fractures. In the section view, the GPR response is typically that of Figure 8c.

The above geometry can be modeled by a vertical stack of point diffractors. The ray-Born synthetic response of Figure 9 shows how the diffraction tails are reinforced by parallel superposition above the steep fracture and weakened by wider spacing and destructive interference below. The real data example in Figure 8a illustrates the moon shape diffraction signature on a time slice. As we add more diffractors, we can observe in Figure 9d that the constructive interference eventually forms a line, and the remainder of the diffraction energy cancels out, except for events at the top and base of this line. This line now represents a reflection; upon migration, the reflector will be located at the diffraction apexes (the migration being time migration and constant background velocity). The events emanating from the top and bottom of the reflector are tip diffractions. Looking again at Figure 8c, we see that the dip of the steep fracture flips from 66° to the northeast to a near-vertical southeast dip in the lower part of the panel. The composite signature contains 10 diffractions distributed over a total fracture length of 3 m, yielding an average spacing of 0.7λ between fracture intersections. The apex depth range is 2 to 8λ.

Combined gentle and steep dip fracture intersection

This example unifies the signatures of the two individual diffraction signatures discussed above. The model, shown in Figure 10a, consists of a 60° dipping steep fracture intersected by several subhorizontal fractures dipping 11° with perpendicular dip azimuth to the steep fracture. This model corresponds to the main intersecting fracture system of the Cassis Quarry. The modeled diffraction signature visible on a time slice, shown in Figure 10b, contains the full geometric information of the quarry fracture network. Here, we are essentially combining the responses of Figures 7 and 9. The dip direction of the subhorizontal fracture set can be directly determined from the diffraction signature; this points toward the smaller circle (which has started later in time). This dip can also be inferred from the hyperbolic images on the time slices, which can be interpreted in an analogous manner to the plunge of an anticline. The dip direction of the steep fracture can be inferred from the spacing of the flanks of the different

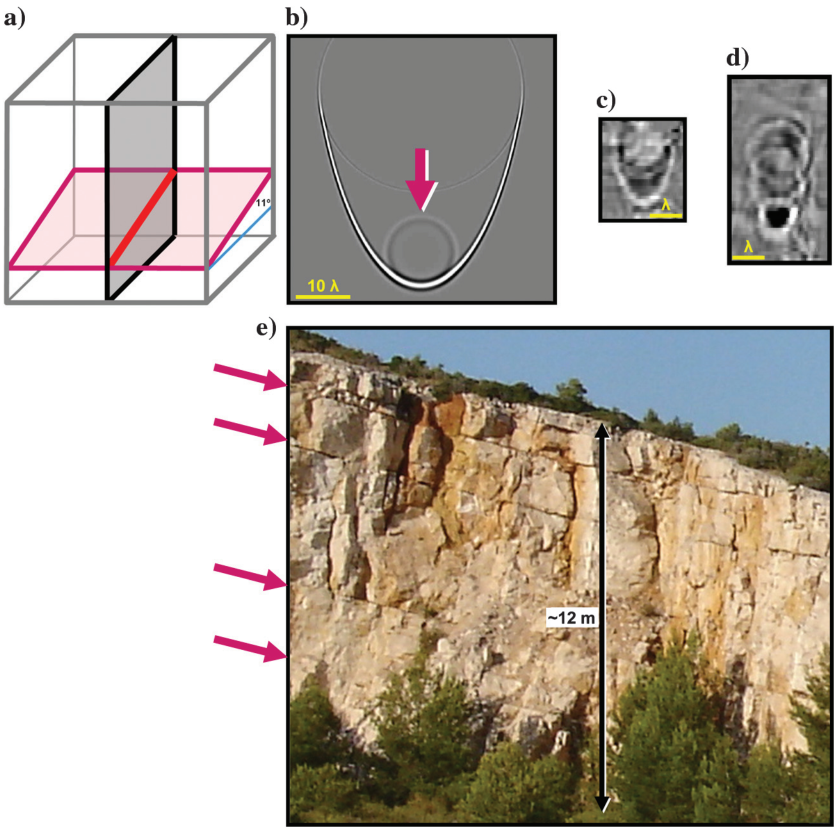

Figure 7. (a) Intersection of a vertical fracture with a 11° dipping subhorizontal fracture. (b) 3D ray-Born synthetic data: dipping line diffractor length $= 32\lambda$, at depths of 10 to 20λ. Time slice extracted two periods below the lowest point of the line diffractor (depth conversion velocity $v = 2000$ m/s and $\lambda = 100$). (c) Single dipping line diffractor in 3D GPR time slice. (d) GPR response of a broken dipping line diffractor consisting of five short line diffractors with an average spacing of 1λ. The dip measured along the apices is 10°. (e) Outcrop photograph in the strike direction of the subhorizontal fracture set.

hyperbolae. Recalling Figure 9, we know that dip is in the direction of the more closely spaced hyperbolae.

The time slice from Figure 10c shows an excellent character match to the synthetic of Figure 10b. The composite diffraction pattern is composed of about 25 individual diffractions. The gentle dip is 12°, and the steep dip is 69° measured along the apexes. The apex depth range is 2 to 5λ. The shallowest part of the signature is shown in Figure 7c, where the steep dip component is not yet evident.

The alternative approach of interpreting the migrated data by tracking alignments of focused diffraction anomalies took many days to complete. The telltale diffraction signatures give away this information on a single unmigrated time slice. Figure 11 shows a 3D overview of the unmigrated Cassis GPR data with steep and subhorizontal fracture interpretations based on migrated data. Here, it must be noted that this interpretation was obtained independently, before the diffraction study. The composite diffraction signature interpretation confirmed the results and was achieved much faster. Our experience in this workflow of interpreting composite diffraction patterns suggests that there is value to working with diffractions before and after migration. By only working with the diffraction-imaged data, we are not fully exploiting the symmetries and organization of the diffraction response.

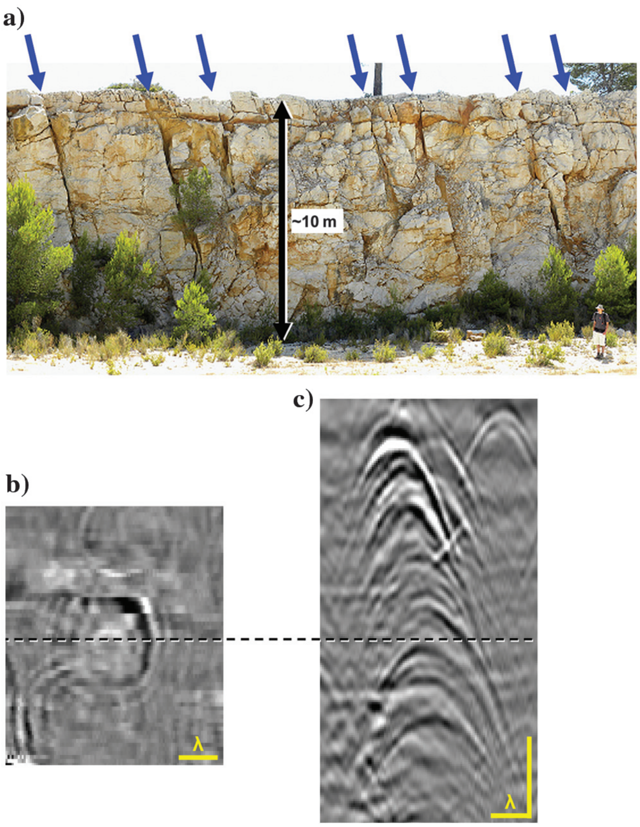

Figure 8. (a) Outcrop photograph of steep dipping fractures intersecting subhorizontal fractures. The outcrop picture is flipped horizontally to match the orientation of vertical sections of Figure 9. (b) 3D GPR time slice. (c) Vertical section. The dotted line between panels (b and c) indicates the figure cut locations.

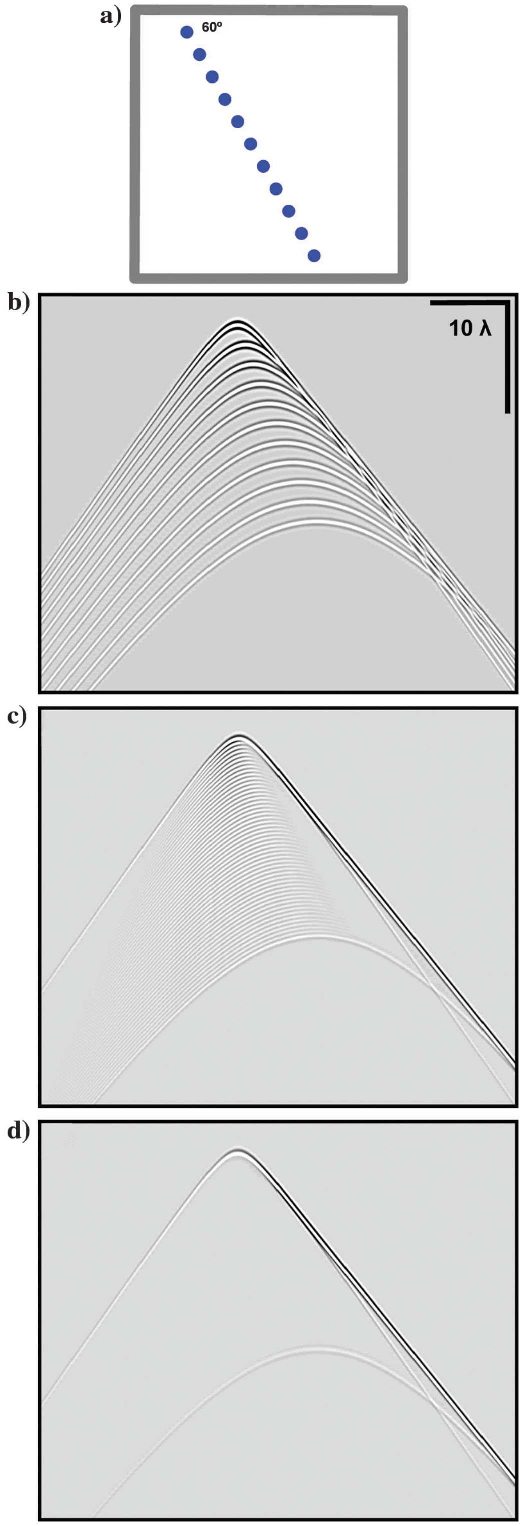

Figure 9. Ray-Born synthetic data of vertically stacked diffractions caused by steep dip fractures. (a) Model with 11 point diffractors on a 60° slope. (b-d) Vertical section of modeled response for 11, 51, and 101 point diffractors, respectively. The point spacing is 2λ, 0.4λ, and 0.2λ.

Similarity of seismic and ground-penetrating radar scale diffractions

Diffractions occur at all scales in the earth, from the GPR scale to the near-surface seismic, exploration seismic, and solid earth scales. For example, at the opposite end of the spectrum from GPR, we have diffractions from the horstlike structure in the core-mantle boundary (see, for example, Phinney and Alexander, 1966; other examples of diffractions at global scale are given in Zhang et al., 2004; Yan and Clayton, 2007). The diffraction phenomena that we observe on GPR data are very similar in character to those seen on the various seismic scales. This is because diffractions at all scales are related by the similarity law of diffraction. The similarity law, related to the dimensionless Fresnel number, was demonstrated in physical experiments by Arkadiew (1913).

As noted by Sommerfeld (1964), "It is often said that diffraction phenomena are noticeable for only very small objects. However, the similarity law says: the same diffraction phenomena observed with a small object are also observed with an object magnified by a similarity transform, provided only that the distances of the source point and point of observation from the object are correspondingly magnified."

For this reason, although the scales involved are very different, the analysis at the GPR data scale can be very useful for understanding diffractions on seismic data. Many of the diffraction patterns will be similar, and with GPR data, we have the advantage of outcrop control.

Upscaling of diffraction responses from outcrop ground-penetrating radar to reservoir depth seismic data

Many clear diffraction signatures have been observed in dense 3D GPR data. Seismic diffraction examples from reservoir depth have been published in recent years. Table 1 compares the GPR and seismic parameters relevant for the detection of diffractions in the near surface and at reservoir depth. The wavelength serves as the scaling link to obtain geometrically equivalent typical seismic and model configurations for which similar diffraction responses as seen in the Cassis GPR data can be expected. By using the wavelength for the definition of diffractor size and depth, we can easily compare GPR, seismic, and synthetic model geometries. Geometric configurations with equal scales in terms of wavelengths produce equal hyperbolic moveout when measured in the time periods of the signal. To facilitate comparisons between the different data modalities, the figures in this paper are annotated with wavelength scales. The model geometries used to compute the synthetic data of Figures 2, 7, 9, and 10 are representative for GPR and seismic scales. The background velocity is 2000 m/s with a center frequency of 20 Hz, resulting in a wavelength of 100 m. The maximum depth of scattering targets is 20λ, with shallower targets in the models including dips. A common observation in the GPR and synthetic data results is that the clearest circular diffraction patterns are visible one to four periods below the apex.

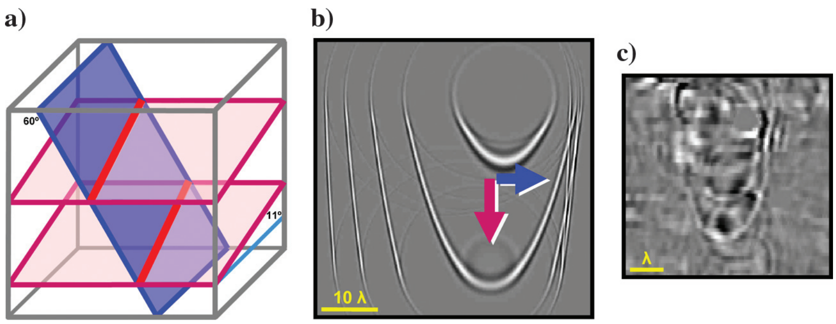

Figure 10. (a and b) Intersection of one subvertical and several 11° dipping subhorizontal fractures causes a diffraction signature from which the dip of subvertical and subhorizontal fractures are evident. (c) Real 3D GPR time-slice example containing the information about the Cassis Quarry main intersecting fracture system.

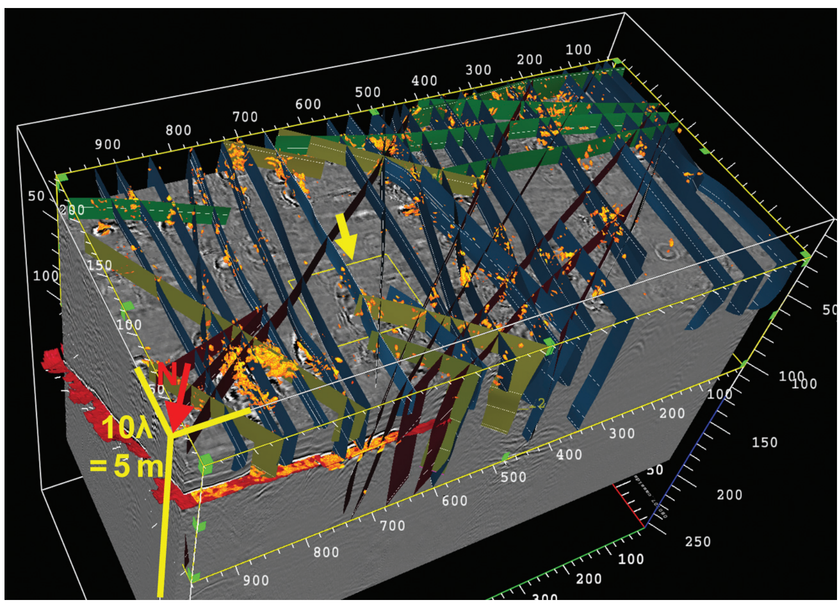

Figure 11. 3D view of the unmigrated Cassis 3D GPR data cube with steep fracture interpretations based on migrated data. The yellow arrow shows the location of the diffraction signature shown in Figure 10c. The orange color shows volume-rendered high-amplitude clusters of 3D migration focused diffractions indicating zones of intense fracturing and karstification.

Table 1. GPR, seismic, and ray-Born model scales.

	GPR in limestone		Seismic in limestone	Model BG = background
Frequency	$f = 200$ MHz		$f = 50$ Hz	$f = 20$ Hz
Velocity	$v_{LST} = 0.1$ m/ns		$v_{LST} = 5000$ m/s	$v_{BG} = 2000$ m/s
Wavelength	$\lambda_{LST} = 0.5$ m		$\lambda_{LST} = 100$ m	$\lambda_{BG} = 100$ m
3D survey gridspacing	0.05 – 0.10 m	→ $\lambda/8 - \lambda/4$ →	12.5 – 25 m	
Fracture segment size forming line- and 3D cross scatterers	0.05 – 2.00 m	→ $\lambda/8 - 4\lambda$ →	12.5 – 400 m	12.5 – 400 m
Max reflection depth	~10 m	→ 20λ	Modeled diffractor depths	$0 - 20\lambda$
Depth range of clear diffractions				
– Mixed refl. and diffr.	0 – 2.5 m	→ $0 - 5\lambda$		
– NO interfering reflections	0 – 5 m	→ $0 - 10\lambda$		

A typical carbonate reservoir velocity of 5000 m/s is chosen. The central frequency of the seismic data is assumed to be 50 Hz. For proper spatial sampling of the full diffraction signals including the dipping diffraction tails, the acquisition trace spacing has to be at least a quarter of the reservoir wavelength (Grasmueck et al., 2005). For 50-Hz seismic arrivals, this translates to 12.5 m. Many recently acquired seismic surveys satisfy this spatial sampling requirement. Our experience with 3D GPR surveys shows that acquiring data with a grid density of an eighth of a wavelength is preferred for unaliased spatial sampling of the high-frequency signal content above the dominant frequency. The length of the fracture intersections creating the line diffractors is 12.5 to 400 m. The combined response from such basic line diffractor elements causes the composite diffraction patterns we show in the GPR and synthetic data examples of this paper. The wavelength scale analogy between GPR and seismic data translates the 1-mm fracture opening observed in outcrop into a 20-cm fracture width at the reservoir level. This means that fractures giving rise to diffractions at GPR scale will not be observed as diffractions at seismic scale. The millimeter joints imaged by GPR will be associated with Mie and Rayleigh scattering at seismic scale (see, for example, Wu, 1989). Larger fractures are usually not clean cuts (Billings, 1954). On the Cassis Quarry walls, only three major faults are exposed besides the omnipresent joints. At closer inspection, the faults do not consist of a single fracture but consist of a narrow zone with intense fracturing (Figure 12). Intersections between such mechanically disturbed sheets with a thickness of 20 cm or more are therefore the likely cause of the diffractions recorded in seismic data. Therefore, it is reasonable to expect similar diffraction signatures for GPR and seismic data.

The comparison of the imaging depths for reflections and diffractions obtained in the Cassis 3D GPR data in Table 1 shows how diffractions are weak signals and only clearly visible in the shallow part. Wherever reflections exist and can be observed, the truncation of a reflector leads to an observable diffraction. This follows from the fact that (specular) reflection describes only part of the backscattered wavefield, and physical continuity considerations demand that there is a smoothing correction in terms of diffraction (Klem-Musatov and Aizenberg, 1985). At the reflector discontinuity, the diffraction has half the amplitude of that of the associated reflection, but away from it, the diffraction quickly decays. As a rule of thumb, seismic diffractions are typically one order of magnitude weaker than reflections (Khaidukov et al., 2004). In the 3D GPR data set used for this paper, there is almost no reflectivity,

a)

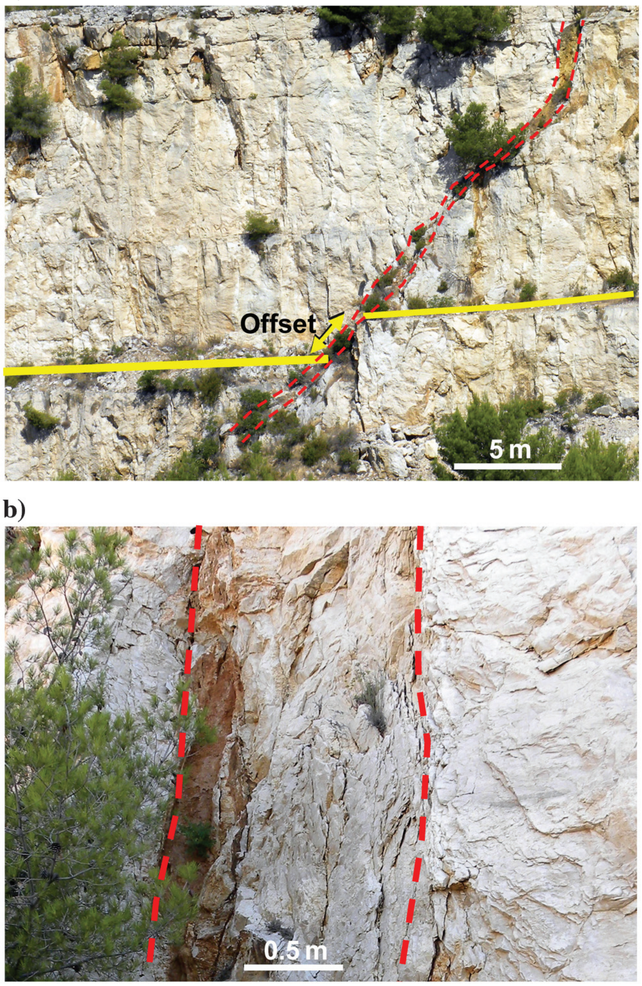

b)

Figure 12. (a) Outcrop photograph of fault with 0.4 to 1.0 m offset. (b) Fault consists of a zone with dense fracturing. Such faults are the seismic scale equivalent of the joints with a 1-mm fracture opening causing GPR diffractions in the Cassis 3D GPR data.

so there is no issue with detection of diffractions and separating them from the main wavefield. Figure 13 shows another unmigrated 3D GPR volume acquired in the same quarry, 120 m to the north. In this survey, the main stratigraphic reflection is offset by a fault (as seen in Figure 12a) with a lateral displacement 0.4 to 1.0 m. Because the fault offset is in the order of one GPR wavelength, the stratigraphic reflection shows a clear discontinuity in the unmigrated and the migrated data. At closer inspection, the unmigrated data reveal a multitude of weak diffractions lining the entire fault, caused by the brittle deformation blocks creating diffractors as shown in Figure 4. With the diffractions, the fault can be also traced away from the stratigraphic reflection. This figure also illustrates the challenge of diffraction imaging; we note that the reflection amplitude is much stronger than that of the diffractions.

In Cassis, we also observe a diffraction amplitude enhancing factor. When we compare amplitudes of diffractions with similar radii in Figure 6, several clusters with stronger amplitudes are evident. Karst dissolution creates voids initiated by fractures. Karst and fractures are discontinuities and cause similar shapes of diffraction signatures. The karst voids have stronger amplitude responses due to their larger opening size and complex shapes with abundant small curvatures (Grasmueck et al., 2013). Figure 11 shows how most of the migrated strong-amplitude karst diffraction clusters are developed at intersections of two or more fractures. The detection of seismic diffractions originating from karst features at reservoir depth is shown by Yang et al. (2011) and Li et al. (2012) in the Tarim Basin.

To see clear diffractions at the reservoir level, special care should be taken during the acquisition, processing and interpretation of seismic data to preserve these very weak signals (Grasmueck et al., 2013): (1) Acquire very dense, vertically stacked single sensor data with a sufficiently high signal-to-noise ratio. Although GPR equipment only has 16 bit dynamic range, the standard 24 bits of seismic analog-to-digital converters are sufficient to also record weak diffraction signals originating at reservoir depth. (2) Preserve all diffracted energy during processing. (3) Separate reflection and diffraction parts of the seismic signal and perform diffraction analysis on the diffraction-only part (Khaidukov et al., 2004).

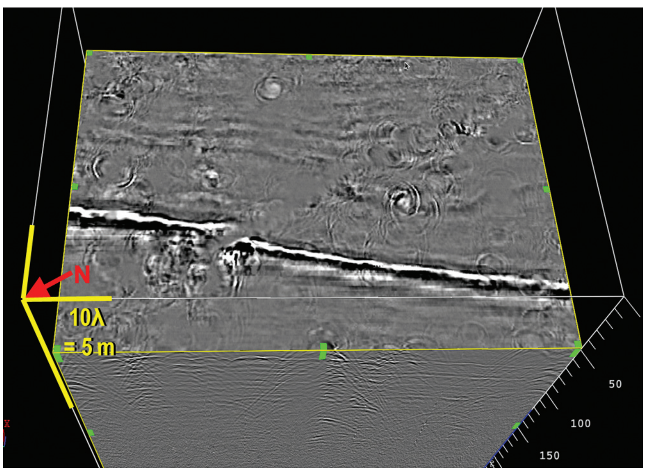

Figure 13 Top view of another Cassis 3D GPR survey imaging the fault shown in Figure 12a. The amplitude of the subhorizontal stratigraphic reflection is much stronger than the diffraction amplitudes. The vertical scale calculated assuming a constant velocity of 0.0975 m/ns.

Salt tectonic seismic data example

In an exploration seismic brute stack cube from the Gulf of Mexico, numerous diffraction circle patterns are visible. Reflectors from a sedimentary basin are truncated by the salt flank. Figure 14a shows a time slice

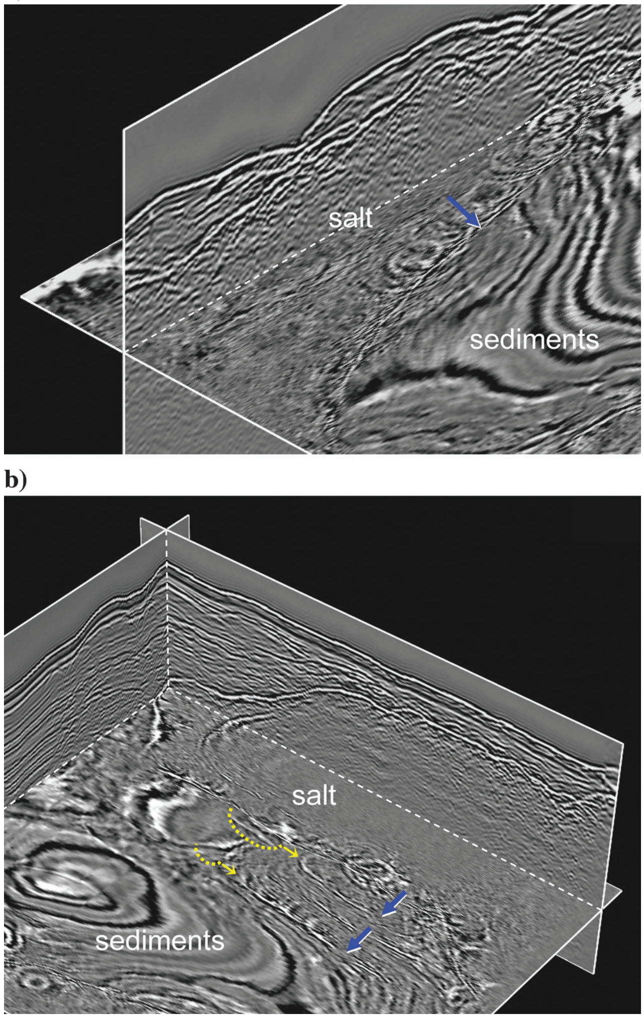

Figure 14. (a) Chair section of an exploration seismic brute stack with diffraction signatures caused by the truncation of a sediment reflector against salt. The time slice depth is 2.2 s. The dip of the stacked diffractors is shown by blue arrow. (b) Two diffraction clusters generated by truncation of two reflectors at different depth toward the salt. The time slice depth is 2.4 s. Yellow dotted curves indicate the size of the diffractions originating at the two sediment-salt truncation levels.

where several diffraction circles overlap with each other, indicating that the line of intersection of the sediments with the salt is not smooth. At first sight, the pattern resembles the GPR signature of Figure 2d with the difference that only one side of the signature is visible. We observe such a one-sided enhancement of diffraction tails by stacking multiple diffractors in a steep dip as shown in Figure 9. The combination of these two basic geometries leads to the interpretation that multiple broken line diffractors are closely stacked in a steep dip against the salt flank. Figure 14b shows another example of such a sediment-salt truncation. Inspection of the deeper time slice shows again one-sided diffraction chains almost parallel to each other. They correspond to the intersections of two different sediment reflectors with the salt flank. The different depth of the intersections is manifested by the different radii of the circles. The shallower sediment-salt intersection is composed of larger circles. Stewart (2006) notes that the line of sediment-salt intersection can be expected to be broken by several radial faults. Rautman et al. (2009) demonstrate for an onshore Gulf Coast diapir that the salt/sediment interfaces and resulting intersection can be much more complex than what is typically represented by seismic based models. Proper identification and correct diffraction imaging can add very important geometric details to salt flank proximity studies. The example in Figure 14 has a center frequency of 35 Hz, demonstrating how diffraction signatures can also be recorded in lower frequency data sets as long as the trace spacing is dense enough to sample the steep diffraction tails in all directions. As discussed in the upscaling section, the size of the imaged diffractors is controlled by the wavelength at target depth. Separate use of diffractions in processing flows can considerably minimize lateral misposition of salt flanks where reflections from the fault planes are difficult to recover due to the very large data acquisition and migration aperture needed and insufficient control of anisotropy. Diffractions are measurable independently from data acquisition and migration aperture (as argued in, e.g., Moser, 2009), and they therefore have very favorable illumination properties compared to reflections. Modeling of broken line and curved-edge diffractors proves to be very helpful in such work flows (Pelissier et al., 2012).

Conclusions

In this paper, we find that besides voids and caverns, fracture intersections are an important source of recordable diffractions in GPR and seismic data. This result is supported by the combined analysis of outcrop observations, high-density 3D GPR imaging, and synthetic ray-Born modeling.

A fracture intersection is represented by a finite-length line diffractor element. Two basic fracture intersection types exist: (1) One single line diffractor element represents two intersecting fractures and (2) three line diffractor elements arranged in a 3D cross represent the intersection of three fractures. The comparison of unmigrated Cassis 3D GPR data with the synthetic model response of long and short line diffractors and 3D crosses leads to the following conclusions:

- Fracture models consisting of flat fracture planes with long straight intersection lines are too simplistic to reproduce the GPR and seismic responses of naturally fractured rock.
- The GPR time slices are dominated by circular diffraction patterns. The linear flanks and tip waves with polarity reversals characteristic for long line diffractions are not commonly observed.
- Most of the diffractions in the 3D GPR data are the response of subwavelength fracture intersections.
- Realistic fracture intersections are broken lines composed of multiple lined-up short line diffractors.
- The response for a quarter-wavelength or shorter line diffractor becomes kinematically indistinguishable from a point diffractor.
- Perfect circular diffractions on GPR time slices are a rare exception. Realistic diffractions are asymmetric, truncated, square, contain amplitude variations, and occur as composite signatures.

These irregularities of natural diffractions are a consequence of the geometry and spacing of intersecting fracture networks generating them. With three simple base-type intersecting fracture models (horizontal dip, gentle dip, and steep dip) and their synthetic diffraction signatures, the Cassis Quarry fracture network geometry can be quickly deciphered from the observed composite diffraction signatures. By applying the same three basic diffraction signatures to a Gulf of Mexico seismic data set, salt tectonic deformation structures of complex salt-sediment intersections can also be interpreted. The nonrandom distribution of sub-Rayleigh size discontinuities is caused by fracture trends and patterns providing information about fracture dip, spacing, and continuity of fractured domains. By their nature, fracture intersections and hence the resulting diffractions are direct indicators of fracture connectivity.

The similarity of diffraction signatures visible at the GPR and seismic scales is supported by the similarity law. The wavelength serves as the scaling link to obtain seismic and GPR subsurface geometries producing similar diffraction patterns. GPR data are therefore a realistic proxy to decipher seismic diffractions. The actual fracture intersection feature in the subsurface generating recordable diffraction depends on the signal wavelength: The millimeter air-filled thin joints of the Cassis Quarry correspond to at least 0.2-m-thick intensely fractured fault zones at the seismic scale. Therefore, the results of diffraction imaging are frequency dependent. Because natural fracture systems follow fractal power law distributions, the imaged geometries are similar for different scales.

Diffractions from fracture intersections exist at all scales and can be recorded at any seismic or GPR frequency. For proper spatial sampling of the steep diffraction tails, the acquisition grid has to be at least a quarter of the target wavelength. Diffraction tails are weak signals. Amplitudes are by an order of magnitude lower than reflections from the same depth. The Cassis 3D GPR data set is an exceptionally clear display of diffractions because there are practically no stratigraphic reflections. Seismic diffractions are often visible in brute stacks over a small offset range. To fully harness diffractions and their information about reservoir fracture systems, seismic data need to be acquired densely with a high signal-to-noise ratio coupled with processing optimized for diffraction signal preservation and separation.

As geophysicists, we are familiar with the diffraction response of basic geologic features such as faults and pinch-outs, as illustrated, for example, by Hilterman (1970, 1975). In this paper, we have illustrated another type of basic model comprised of spatially organized sets of short line diffractors caused by fracture intersections, providing a compelling character tie to the GPR real data. The same approach can be extended to apply to seismic data.

Acknowledgments

This research is supported by the Sponsors of the Center for Carbonate Research (CSL) at the University of Miami and the National Science Foundation (Grant No. 0323213 and No. 0440322). The University of Miami acknowledges the support of this research by Landmark Graphics Corporation via the Landmark University Software Grant Program. We are grateful to J. LaMarche, F. Fournier, J. P. Borgomano, J. P. Masse, and the City of Cassis for facilitating access to the quarry and support during fieldwork and geological interpretation. We thank Western Geco for permission to present a real seismic data case from the Gulf of Mexico. E. Landa, G. Tsoflias, and an anonymous reviewer are thanked for the constructive feedback to improve the manuscript.

References

Arkadiew, W., 1913, Die Fresnelschen Beugungserscheinungen: Physikalische Zeitschrift, **14**, 832–835.

Besicovitch, A. S., and H. D. Ursell, 1937, Sets of fractional dimensions: Journal of the London Mathematical Society, **12**, 18–25, doi: 10.1112/jlms/s1-12.45.18.

Billings, M. P., 1954, Structural geology, second edition: Prentice-Hall, Inc.

Dong, L., Z. Yao, G. F. Margrave, and E. V. Gallant, 1999, Simulating measurements from physical modeling by Kirchhoff diffraction method: CREWES Research Report, 11.

Geiser, P., A. Lacazette, and J. Vermilye, 2012, Beyond 'dots in a box': An empirical view of reservoir permeability with tomographic fracture imaging: First Break, **30**, 63–69.

Grasmueck, M., M. Coll, G. P. Eberli, and K. Pomar, 2013, Diffraction imaging of sub-vertical fractures and karst with full-resolution 3D ground-penetrating radar: Geophysical Prospecting, **61**, 907–918, doi: 10.1111/1365-2478.12004.

Grasmueck, M., R. Weger, and H. Horstmeyer, 2005, Full-resolution 3-D GPR imaging: Geophysics, **70**, no. 1, K12–K19, doi: 10.1190/1.1852780.

Hilterman, F. J., 1970, Three-dimensional seismic modeling: Geophysics, **35**, 1020–1037, doi: 10.1190/1.1440140.

Hilterman, F. J., 1975, Amplitudes of seismic waves — A quick look: Geophysics, **40**, 745–762, doi: 10.1190/1.1440565.

Khaidukov, V., E. Landa, and T. J. Moser, 2004, Diffraction imaging by focusing and defocusing: An outlook on seismic superresolution: Geophysics, **69**, 1478–1490, doi: 10.1190/1.1836821.

Klem-Musatov, K. D., and A. M. Aizenberg, 1985, Seismic modeling by methods of the theory of edge waves: Journal of Geophysics, **57**, 90–105.

Landa, E., V. Shtivelman, and B. Gelchinsky, 1987, A method for detection of diffracted waves on common-offset sections: Geophysical Prospecting, **35**, 359–373, doi: 10.1111/j.1365-2478.1987.tb00823.x.

Li, F., B. Di, J. Wei, and X. Li, 2012, Volume estimation of the carbonate fracture-cavern reservoir — A physical model study: 74th Annual International Conference and Exhibition, EAGE, Extended Abstracts, A007.

López-Martinez, C., L. Ferro-Famil, and E. Pottier, 2005, Tutorial on SAR polarimetry: The polarimetric SAR data processing and educational tool, https://earth.esa.int/web/polsarpro/polarimetry-tutorial, accessed 13 March 2014.

Malcolm, A. E., M. V. de Hoop, and B. Ursin, 2011, Recursive imaging with multiply scattered waves using partial image regularization: A North Sea case study: Geophysics, **76**, no. 2, B33–B42, doi: 10.1190/1.3537822.

Marfurt, K. J., R. L. Kirlin, S. L. Framer, and M. S. Bahorich, 1998, 3-D seismic attributes using a semblance-based coherency algorithm: Geophysics, **63**, 1150–1165, doi: 10.1190/1.1444415.

Masse, J. P., M. Fenerci, and E. Pernarcic, 2003, Palaeobathymetric reconstruction of peritidal carbonates Late Barremian, Urgonian sequences of Provence (SE France): Palaeogeography, Palaeoclimatoly, Palaeoecology, **200**, 65–81, doi: 10.1016/S0031-0182(03)00445-0.

Moser, T. J., 2009, Diffraction imaging in subsalt geometries and a new look at the scope of reflectivity: EAGE Subsalt Imaging Workshop, Extended Abstracts, SS22.

Moser, T. J., 2010, Review of ray-Born forward modeling for migration: 72nd Annual International Conference and Exhibition, EAGE, Extended Abstracts, G035.

Moser, T. J., 2012, Review of ray-Born forward modeling for migration and diffraction analysis: Studia Geophysica et Geodaetica, **56**, 411–432, doi: 10.1007/s11200-011-9046-0.

Pant, D. R., S. A. Greenhalgh, and B. Zhou, 1992, Physical and numerical model study of diffraction effects on seismic profiles over simple structures: Geophysical Journal International, **108**, 906–916, doi: 10.1111/j.1365-246X.1992.tb03479.x.

Pelissier, M. A., T. J. Moser, M. Grasmueck, and J. Pajchel, 2012, Three-dimensional diffraction response of salt diapirs: 74th Annual International Conference and Exhibition, EAGE, Extended Abstracts, Y029.

Phinney, R. A., and S. S. Alexander, 1966, P-wave diffraction theory and the structure of the core-mantle boundary: Journal of Geophysical Research, **71**, 5959–5975, doi: 10.1029/JZ071i024p05959.

Questiaux, J. M., G. D. Couples, and N. Ruby, 2010, Fractured reservoirs with fracture corridors: Geophysical Prospecting, **58**, 279–295, doi: 10.1111/j.1365-2478.2009.00810.x.

Rautman, C. A., K. M. Looff, and K. M. Looff, 2009, Three-dimensional geometric model of the Bayou Choctaw salt dome, southern Louisiana, using 3-D seismic data: Sandia National Laboratories, Publication SAN, D2009–1037.

Sánchez-Sesma, F. J., and U. Iturrarán-Viveros, 2001, Scattering and diffraction of SH waves by a finite crack: An analytical solution: Geophysical Journal International, **145**, 749–758, doi: 10.1046/j.1365-246x.2001.01426.x.

Sommerfeld, A., 1964, Lectures on theoretical physics: Optics: Academic Press, Inc.

Stewart, S. A., 2006, Implications of passive salt diapir kinematics for reservoir segmentation by radial and concentric faults: Marine and Petroleum Geology, **23**, 843–853, doi: 10.1016/j.marpetgeo.2006.04.001.

Thore, P., R. Gibson, V. Lisitsa, G. Reshetova, and V. Tcheverda, 2009, Accurate generation of seismograms on fractured reservoirs: International Petroleum Technology Conference, 13910.

Thore, P., and I. Tarrass, 2010, Accurate modeling of fractured reservoir not using equivalent medium theory: 72nd Annual International Conference and Exhibition, EAGE Extended Abstracts, P593.

Wu, R. S., 1989, Seismic wave scattering, *in* D. James ed., Encyclopedia of geophysics: Van Nostrand Reinhold and Company, 1166–1187.

Yan, Z., and R. W. Clayton, 2007, A notch structure on the Moho beneath the Eastern San Gabriel Mountains: Earth and Planetary Science Letters, **260**, 570–581, doi: 10.1016/j.epsl.2007.06.017.

Yang, P., Y. L. Liu, H. Y. Li, G. J. Dan, H. T. An, and Y. M. Shao, 2011, Fractured-vuggy reservoir characterization of carbonate, Tarim Basin, Northwest China: 73rd Annual International Conference and Exhibition, EAGE, Extended Abstracts, P116.

Zhang, Z. J., Y. L. Qin, Y. Chen, C. Y. Zhang, S. X. Sun, B. Zhao, Y. F. Liu, and Z. K. Liu, 2004, Reconstruction of semblance section for the crust/mantle reflection structure by wide-angle seismic data: Chinese Journal of Geophysics, **47**, 533–538, doi: 10.1002/cjg2.517.

Mark Grasmueck received M.S. (1991) and Ph.D. (1995) degrees in geophysics from ETH Zürich, Switzerland. He worked as an exploration geophysicist for Shell International in the Netherlands for four years. Since 2000, he has been a faculty member of the Department of Marine Geosciences at the Rosenstiel School of Marine and Atmospheric Science, the University of Miami, Florida (USA). His research interests include development and integration of efficient and highly resolving GPR and seismic methods for noninvasive 3D and 4D imaging of natural environments. He is pursuing applications in carbonate reservoir characterization, imaging of fractures and karst, tracking and quantification of fluid flow, archeological mapping, and characterization of deep-water coral ecosystems. He is a member of SEG, AGU, AAPG, EAGE, and EEGS.

Tijmen Jan Moser received a Ph.D. from Utrecht University and has worked as a geophysical consultant for a number of companies and institutes (Amoco, Institut Français du Pétrole, Karlsruhe University, Bergen University, Norsk Hydro, Geophysical Institute of Israel, Fugro-Jason, and Horizon Energy Partners). For the past few years, he has been working independently. His main interests include seismic imaging, asymptotic methods, and diffractions, in which he has authored many influential papers. He is the editor-in-chief of *Geophysical Prospecting*, a member of SEG and MAA, and an honorary member of EAGE.

Michael A. Pelissier received a B.S. in geophysics from the State University of New York at Binghamton, an M.S. in geophysics from the Colorado School of Mines, and a Ph.D. in geophysics from the University of London. He joined the industry in 1979 and has held various positions focused on seismic interpretation and reservoir characterization with Marathon Oil Company, CGG and Phillips Petroleum Company. He is a consulting geophysicist with Roc Oil (Bohai) Company, based in Beijing. His interests include quantitative interpretation workflows for field development and reservoir management, with an emphasis on integrating geoscience and reservoir engineering disciplines. He has co-edited *Classics of Elastic Wave Theory* and also a member of SEG and EAGE.